ISSN 1674-1056
http://cpb.iphy.ac.cn
http://iopscience.iop.org/cpb
中国物理 B
Chinese Physics
中国物理
Chinese Physics B

Giant Rashba-like spin-orbit splitting with distinct spin texture in two-dimensional heterostructures

Jianbao Zhu(朱健保), Wei Qin(秦维), and Wenguang Zhu(朱文光)

Citation: Chin. Phys. B, 2021, 30 (**8**): 087307. DOI: 10.1088/1674-1056/ac0784
Journal homepage: http://cpb.iphy.ac.cn; http://iopscience.iop.org/cpb

What follows is a list of articles you may be interested in

Fabrication of sulfur-doped cove-edged graphene nanoribbons on Au(111)

Huan Yang(杨欢), Yixuan Gao(高艺璇), Wenhui Niu(牛雯慧), Xiao Chang(常霄), Li Huang(黄立), Junzhi Liu(刘俊治), Yiyong Mai(麦亦勇), Xinliang Feng(冯新亮), Shixuan Du(杜世萱), and Hong-Jun Gao(高鸿钧)
Chin. Phys. B, 2021, 30 (**7**): 077306. DOI: 10.1088/1674-1056/abfbd0

A first-principles study on zigzag phosphorene nanoribbons terminated by transition metal atoms

Shuai Yang(杨帅), Zhiyong Wang(王志勇), Xueqiong Dai(戴学琼), Jianrong Xiao(肖剑荣), and Mengqiu Long(龙孟秋)
Chin. Phys. B, 2021, 30 (**2**): 027305. DOI: 10.1088/1674-1056/abc0e1

General principles to high-throughput constructing two-dimensional carbon allotropes

Qing Xie(谢庆), Lei Wang(王磊), Jiangxu Li(李江旭), Ronghan Li(李荣汉), Xing-Qiu Chen(陈星秋)
Chin. Phys. B, 2020, 29 (**3**): 037306. DOI: 10.1088/1674-1056/ab6c4b

Hydrogenated antimonene as quantum spin Hall insulator: A first-principles study

Xin He(贺欣), Ji-Biao Li(李佶彪)
Chin. Phys. B, 2019, 28 (**3**): 037301. DOI: 10.1088/1674-1056/28/3/037301

Quantum spin Hall insulators in chemically functionalized As (110) and Sb (110) films

Xiahong Wang(王夏烘), Ping Li(李平), Zhao Ran(冉召), Weidong Luo(罗卫东)
Chin. Phys. B, 2018, 27 (**8**): 087305. DOI: 10.1088/1674-1056/27/8/087305

Giant Rashba-like spin–orbit splitting with distinct spin texture in two-dimensional heterostructures*

Jianbao Zhu(朱健保)[1,2], Wei Qin(秦维)[2], and Wenguang Zhu(朱文光)[1,2,†]

[1] Department of Physics, University of Science and Technology of China, and Key Laboratory of Strongly-Coupled Quantum Matter Physics, Chinese Academy of Sciences, Hefei 230026, China

[2] International Center for Quantum Design of Functional Materials (ICQD), Hefei National Laboratory for Physical Sciences at the Microscale, and Synergetic Innovation Center of Quantum Information and Quantum Physics, University of Science and Technology of China, Hefei 230026, China

(Received 2 May 2021; revised manuscript received 27 May 2021; accepted manuscript online 3 June 2021)

Based on first-principles density functional theory calculation, we discover a novel form of spin–orbit (SO) splitting in two-dimensional (2D) heterostructures composed of a single Bi(111) bilayer stacking with a 2D semiconducting In_2Se_2 or a 2D ferroelectric α-In_2Se_3 layer. Such SO splitting has a Rashba-like but distinct spin texture in the valence band around the maximum, where the chirality of the spin texture reverses within the upper spin-split branch, in contrast to the conventional Rashba systems where the upper branch and lower branch have opposite chirality solely in the region below the band crossing point. The ferroelectric nature of α-In_2Se_3 further enables the tuning of the spin texture upon the reversal of the electric polarization with the application of an external electric field. Detailed analysis based on a tight-binding model reveals that such SO splitting texture results from the interplay of complex orbital characters and substrate interaction. This finding enriches the diversity of SO splitting systems and is also expected to promise for spintronic applications.

Keywords: spin–orbit splitting, two-dimensional heterostructure, first-principles calculation

PACS: 73.20.–r, 71.15.Mb, 71.70.Ej **DOI:** 10.1088/1674-1056/ac0784

1. Introduction

Manipulating and exploiting the spin degree of freedom of electron as the information carrier, especially with electrical controllability, is one of the central themes in the growing field of spintronics,[1,2] which critically relies on the spin splitting of the electronic bands in the vicinity of the fundamental semiconductor gap. Among a variety of proposes, spin–orbit (SO) coupling mechanisms provide a potentially effective approach for this purpose. Apart from the conventional magnetic systems where the spin degeneracy is lifted by time reversal symmetry breaking, SO coupling has also been demonstrated to be able to induce momentum-dependent band spin splitting in spatial inversion asymmetric systems. According to the forms of inversion asymmetry, SO splitting has two most prominent categories, Dresselhaus type occurring in bulk inversion asymmetric[3] and Rashba type in structural inversion asymmetric systems.[4] More recently, some other SO splitting mechanisms were also discovered in various systems.[5–8] The different SO splitting mechanisms result in distinct spin textures of the energy bands in the momentum space, which is expected to lead to different behaviors of spin transport. In particular, stimulated by the seminal work of Datta and Das on the proposal of spin field-effect transistor based on the characteristic spin texture of Rashba SO splitting, extensive efforts have been devoted to searching for large Rashba SO splitting systems,[9] such as semiconductor heterostructures,[10] surface systems,[11,12] and polar materials.[13–15] However, discovering new forms of SO splitting may provide more alternative approaches to control spin transports for the design of spintronic devices and also be of fundamental interest.

The general form of the single-band Rashba-type Hamiltonian is expressed as $H_{\mathrm{R}} = \alpha(k_x\sigma_y - k_y\sigma_x)$, which leads to the well-known "spin-momentum locking" effect, forming chiral spin-split bands. For realistic materials, the "spin" defined in the above Hamiltonian is usually not the real electron spin, but the total angular momentum $\boldsymbol{J} = \boldsymbol{L} + \boldsymbol{S}$, which is the combination of the real spin $\boldsymbol{S}$ and the orbital angular momentum $\boldsymbol{L}$, due to SOC. The basis of the Hamiltonian are denoted as $|\psi_{J_z=\pm 1/2}\rangle$, where $\pm 1/2$ represents the total angular momentum along the z direction. When considering a single band such as p_z orbital that has zero z-direction angular momentum, $|\psi_{J_z=\pm 1/2}\rangle$ reduce to $|\uparrow,\downarrow\rangle$. This model gives rise to the conventional Rashba spin texture as shown in Fig. 1(l). However, when involving p_x and p_y orbitals that also have nonezero z-direction angular momentum, the resultant spin texture will be more complex, and different orbitals will lead to spin texture with different chiralities.[16–19] Based on such multi-

*Project supported by the Science Fund from the Ministry of Science and Technology of China (Grant Nos. 2017YFA0204904 and 2019YFA0210004), the National Natural Science Foundation of China (Grant Nos. 11674299 and 11634011), the Strategic Priority Research Program of the Chinese Academy of Sciences (Grant No. XDB30000000), the Fund of Anhui Initiative Program in Quantum Information Technologies (Grant No. AHY170000), and the Fundamental Research Funds for the Central Universities, China (Grant No. WK3510000013).

†Corresponding author. E-mail: wgzhu@ustc.edu.cn

© 2021 Chinese Physical Society and IOP Publishing Ltd

band nature of the general Rashba model, more complex spin texture that involves a variation of chirality within one band may emerge in materials with competition in different orbital characters.

In this paper, based on the first-principles density functional theory (DFT) calculations, we report a novel form of SO splitting in van der Waals 2D heterostructures composed of a single Bi(111) bilayer stacking with a 2D semiconducting In_2Se_2 or a 2D ferroelectric α-In_2Se_3 layer. With the help of substrate interaction, a complex orbital texture leads to a novel spin texture. Such novel SO splitting exhibits a similar helical spin polarization in the in-plane momentum space as the typical Rashba SO splitting, characterized by the appearance of two spin–momentum locked sub-bands with opposite chirality in the constant energy surface (CES). However, this CES is cut above the band-crossing point in our system owing to the reversal of chirality within the upper spin-split branch, while in the typical Rashba system, similar texture appears in the CES below the band-crossing point due to the the reversal of chirality from the upper spin-split branch to the lower one. The ferroelectric nature of α-In_2Se_3 further allows to tune such SO splitting upon the reversal of its electric polarization with the application of an external electric field. A simplified tight-binding model reveals that such SO splitting texture is attributed to its strong coupling with the orbital texture dictated by the orbit-dependent hybridization between the conduction band of the Bi layer and the valence bands of the In_2Se_2 or In_2Se_3 layer.

2. Methods

Our DFT calculations were performed using the Vienna *ab initio* simulation package (VASP).[20] The wavefunctions of valence electrons are expanded by projector-augmented-wave method[21,22] with a 300-eV plane-wave energy cutoff. Perdew–Burke–Ernzerhof[23] (PBE) parameterization of generalized gradient approximation (GGA) and DFT-D3[24] correction for van der Walls (vdW) interaction are used to determine the structure and total energy. The hybrid functional (HSE06) method[25] along with fully relativistic formalism were applied to obtain accurate band structures with the effects of the SO coupling included. The whole system was simulated in a slab with a vacuum region of more than 15 Å and a saw-like dipole layer was placed in the middle of the vacuum region in order to remove the potential mismatch on the two surfaces of the 2D heterostructures due to the intrinsic electric polarization. A Γ-centered $12 \times 12 \times 1$ Monkhorst–Pack[26] $\boldsymbol{k}$-mesh was used for $\boldsymbol{k}$-point sampling and optimal structure will not be achieved until the forces on each atom are all less than 0.005 eV/Å.

3. Results and discussion

3.1. Reversed spin-texture chirality from first-principles calculations

The proposed van der Waals 2D heterostructures consist of a single Bi(111) bilayer with an In_2Se_2 or an α-In_2Se_3 layer. The single Bi(111) bilayer (Bi bilayer for short), viewed as isolated from its rhombohedral bulk structure along the (111) plane, has a buckled honeycomb structure with the atoms in two triangular sublattices vertically separated into two atomic layers. Recent experiments have demonstrated successful growth of Bi bilayers on a variety of van der Waals substrates.[27–31] Both In_2Se_2 and α-In_2Se_3 have similar layered bulk structures with van der Waals stacking, and each covalently bonded layer contains four and five atomic layers, respectively, but both with only one elemental species in each atomic layer arranged in a triangular lattice. Each In_2Se_2 layer simply follows an atomic-layer stacking sequence of ABBA (A, B, and C are three high-symmetry sites of a triangle lattice as illustrated in Fig. 2(a)) with a corresponding species order of Se–In–In–Se.[32] The structure of α-In_2Se_3 is slightly more complicated due to its ferroelectric nature.[33–38] Each α-In_2Se_3 layer contains five atomic layers in a species order of Se–In-Se–In–Se but follows a stacking sequence of either ABBCA or ABCCA. These two configurations, differing by a seemingly lateral shift of the central Se layer, are completely equivalent, but corresponding to two oppositely polarized ferroelectric states. The in-plane lattices of the Bi bilayer, In_2Se_2, and α-In_2Se_3 possess the same symmetry and similar lattice constants of $a = b = 4.411$ Å, 4.074 Å, and 4.105 Å, respectively, which yields acceptable lattice mismatch between Bi bilayer and In_2Se_2 or α-In_2Se_3 of about 7% for van der Waals heterostructures.[39,40] To accommodate the lattice mismatch, we chose $a = b = 4.10$ Å as the in-plane lattice constant for all heterostructures in our calculations. Figure 1(a) shows the optimized stable structure of the Bi-bilayer/In_2Se_2 heterostructure, and figures 1(b) and 1(c) show the Bi-bilayer/α-In_2Se_3 heterostructures with the electric polarization of the α-In_2Se_3 layer pointing upward and downward, respectively. The calculated interlayer binding energies between the Bi bilayer and the substrates in the above three cases are 0.23 eV, 0.20 eV, and 0.19 eV per unit cell, respectively. These values are larger than the energy cost of a Bi bilayer under a 7% in-plane compressive strain (about 0.1 eV), and thus Bi bilayer and In_2Se_2 or α-In_2Se_3 may form lattice-matched heterostructures, as experimentally demonstrated in the case of Bi bilayer grown on Bi_2Se_3.[29]

Before discussing the electronic structures of the heterostructures, we first show the band structures of the isolated systems as a reference. As displayed in Figs. 1(d)–1(f), the pristine Bi bilayer, In_2Se_2, and α-In_2Se_3 monolayers are all

semiconductors with calculated band gaps of 0.12 eV, 2.11 eV, and 1.46 eV, respectively. As a Bi bilayer stacks with an In_2Se_2 or an α-In_2Se_3 layer, the formed heterostructures remain semiconductors as shown in Figs. 1(g)–1(i). But it is noteworthy that, in both Bi-bilayer/In_2Se_2 (Fig. 1(g)) and Bi-bilayer/α-In_2Se_3-dipole-upward (Fig. 1(h)) heterostructures, the energy bands at the vicinity of the top of the valence band around the Γ point exhibit a signature of double-parabolic-band pattern as normally observed in typical Rashba SO splitting systems, as illustrated in Fig. 1(l).

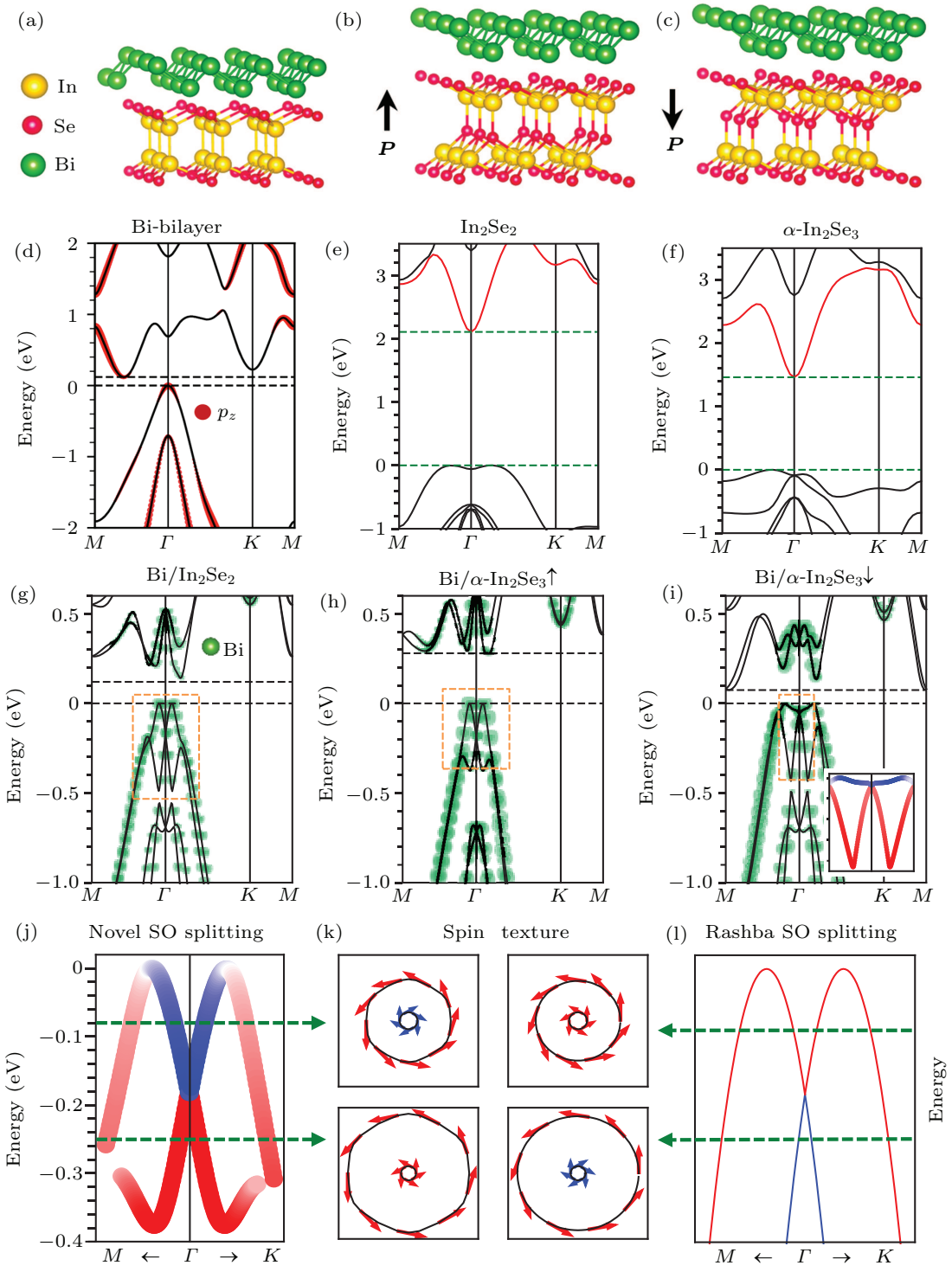


Fig. 1. (a)–(c) Structures of Bi-bilayer/In_2Se_2 (a), Bi-bilayer/α-In_2Se_3-dipole-upward (b), and Bi-bilayer/α-In_2Se_3-dipole-downward (c) heterostructures. The black arrows in panels (b) and (c) indicate the orientation of the out-of-plane electric polarization of the α-In_2Se_3 substrate. (d)–(f) Band structures of pristine Bi-bilayer (d), In_2Se_2 monolayer (e), and α-In_2Se_3 monolayer. Red lines in panels (e) and (f) indicate the conduction band. The dashed lines indicate the band edges. (g)–(i) Band structures of the three heterostructures (a)–(c). The orange dashed rectangles in panels (g)–(i) highlight the areas for showing spin texture and the green dots in the bands represent the atomic contribution of Bi atoms. Insert in panel (i) shows its spin texture. (j) and (l) Spin textures of the region highlighted in panel (h) and a typical Rashba SO splitting, respectively. Red and blue colors represent right-handed and left-handed chirality of the spin texture, respectively. (k) In-plane spin textures respectively taken at the constant energies above and below the band-crossing points as indicate by the green dashed lines in panels (j) and (l).

However, detailed analysis on the spin textures of the energy bands indicates that the nature of this pattern is completely different from the Rashba SO splitting and this new form of splitting cannot be understood in the framework of the conventional Rashba's picture. As revealed previously, the Rashba SO splitting is formed by a lateral split of a single parabolic spin-degenerate energy band into two spin-split branches, both of which show a helical spin texture, resulting in two circular chiral sub-bands in the CES. The most commonly referred feature of the Rashba SO splitting is the two circular sub-bands possessing opposite chirality. Such feature, as illustrated in the right part of Fig. 1(k), is also shown in the Bi-bilayer/In_2Se_2 and Bi-bilayer/α-In_2Se_3-dipole-upward heterostructures, in which a clockwise circular inner sub-band coincides with an anti-clockwise slightly warped outer sub-band (the left part of Fig. 1(k)). However, the key difference is that the reversal of chirality only occurs in the CES taken below the band-crossing point where the inner and outer circular bands belong to the lower and upper spin-split branches, respectively, in the conventional Rashba systems (Fig. 1(l)), while such reversal occurs in the CES taken above the band-crossing point where both the inner and outer circular bands belong the upper spin-split branches in our systems (Fig. 1(j)). Therefore, the spin textures in our heterostructures are radically different from the ones in the typical Rashba systems, and such a novel form of SO splitting has not been reported in the literature to the best of our knowledge. We also examined the effects of an external out-of-plane electric field on the observed SO splitting. The variations of the energy difference between the maximum of the valence band and the band crossing point are merely on order of meV at an electric field of 0.1 eV/Å, which are much less smaller than the absolute values of the SO splitting induced by the proposed substrates. On the other hand, as the electric polarization of the α-In_2Se_3 layer is switched to pointing downward, the band structure (Fig. 1(i)) is dramatically changed and its spin texture as shown in the inset of Fig. 1(i) indicates Rashba nature. The variation of the spin texture upon the reversal of the electric polarization of the underlying α-In_2Se_3 substrate is also radically different from the case of the ferroelectric Rashba system such as GeTe (Ref. [14]), where the reversal of the electric polarization simply flips the chirality of the spin-split bands.

3.2. Band evolution analysis based on a tight-binding model

To unravel the underlying physical mechanism of the discovered SO splitting pattern, we propose a tight-binding model in the framework of the Slater–Koster method. By comparing the band structures of the heterostructures and the isolated system and analyzing the atomic contribution of the energy bands, we find that the bands of interest are mainly derived from the valence band of the Bi bilayer and the conduction bands of the In_2Se_2 and α-In_2Se_3 layers. In this regard, the $3s$, $3p_x$, $3p_y$, and $3p_z$ orbitals of Bi are included in the tight-binding model. For the In_2Se_2 and α-In_2Se_3 substrate, we simply consider its conduction band in the form of effective mass approximation as

$$\hat{H}_{\rm IS}|\phi_{\rm IS}\rangle = \frac{\hbar^2 k^2}{2m^*}|\phi_{\rm IS}\rangle. \tag{1}$$

The Hamiltonian of the heterostructure can be generally written as

$$H = \begin{pmatrix} H_{\rm Bi} & H_1 \\ H_1^\dagger & H_{\rm IS} \end{pmatrix} + h_{\rm so}, \tag{2}$$

where $H_{\rm Bi}$ and $H_{\rm IS}$ are the Bi bilayer and the substrate parts and H_1 and $h_{\rm so}$ describes the interlayer interaction and spin orbit coupling, respectively. As illustrated in Fig. 2(a), up to second-neighbor interaction between the Bi atoms and nearest-neighbor interaction between the interfacial Bi and Se atoms are considered. The SO coupling is described by the on-site $\boldsymbol{L}\cdot\boldsymbol{S}$ term as

$$h_{\rm so} = \lambda_{\rm R}\boldsymbol{L}\cdot\boldsymbol{S}. \tag{3}$$

Based on this model, the DFT band structure can be well reproduced as shown in Fig. 2(f). In the following, we demonstrate the evolution of the band structure upon the variation of two key parameters $\lambda_{\rm R}$ and $V_{\rm IS}$, which describe the SO coupling and interlayer interaction, respectively. Initially, when both $\lambda_{\rm R}$ and $V_{\rm IS} = 0$, the band structure is simply the superposition of overlapping valence band of the Bi bilayer and conduction band of the substrate (Fig. 2(b)). The VB1 and VB2 bands, denoted by $p_{x\pm{\rm i}y}$, are degenerate at the Γ point, due to the in-plane two-fold degeneracy ($l = 1$, $m = \pm 1$). When the interlayer interaction $V_{\rm IS}$ is turned on to be 0.3 eV, the hybridization between the CB1 and the VB1 bands leads to a gap opening at the band-crossing point A (Fig. 2(c)). However, the CB1 band essentially has no hybridization with the VB2 band. The orbital-projected band structure indicates the VB2 band is mainly composed of in-plane p_x and p_y orbitals, the overlap integrals of this band with the CB1 band of the substrate is nearly neglectable. In additional, the interlayer interaction does not break the in-plane two-fold degeneracy, and thus the VB1 and the VB2 bands are still degenerate at the Γ point, labeled as B point in Fig. 2(c). Next, when a weak SO coupling ($\lambda_{\rm R} = 0.1$ eV) is applied, as illustrated in Fig. 2(g), $p_{x\pm{\rm i}y}$ split into higher ($J_z = \pm 3/2$) and lower ($J_z = \pm 1/2$) spin states, and the spin degeneracy is lifted due to the space inversion symmetry breaking (Fig. 2(d)). Meanwhile, a new gap is opened at the band-crossing point C due to a synergistic effect of the hybridization of the CB1 band and the p_z orbital dominated VB2 band with the SO coupling. Interestingly, with the increase of the SO coupling strength, the C1 point goes upward, the C2 and B point go downward, and eventually the band structure with a similar dispersion pattern as the DFT

results is achieved at $\lambda_R = 0.8$ eV (Fig. 2(f)). Although as shown in Fig. 2(g), a band inversion takes place between p_z^- and the higher spin state, the valence band around the Γ point largely maintain the lower spin state in the basis composed of $|p^+_{x+\mathrm{i}y,\downarrow}, p^+_{x-\mathrm{i}y,\uparrow}, p^+_{z,\downarrow}, p^+_{z,\uparrow}\rangle$. Therefore, the novel spin splitting state here can be well described by the basis of $|\psi_{J_z=\pm1/2}\rangle$. On the other hand, when the strength of V_{IS} increases from 0.1 eV to 0.3 eV, spin splitting also becomes larger. Therefore, both the strong atomic SOC of Bi and the interlayer interaction are responsible for the achieved giant Rashba-like SO splitting in our systems.

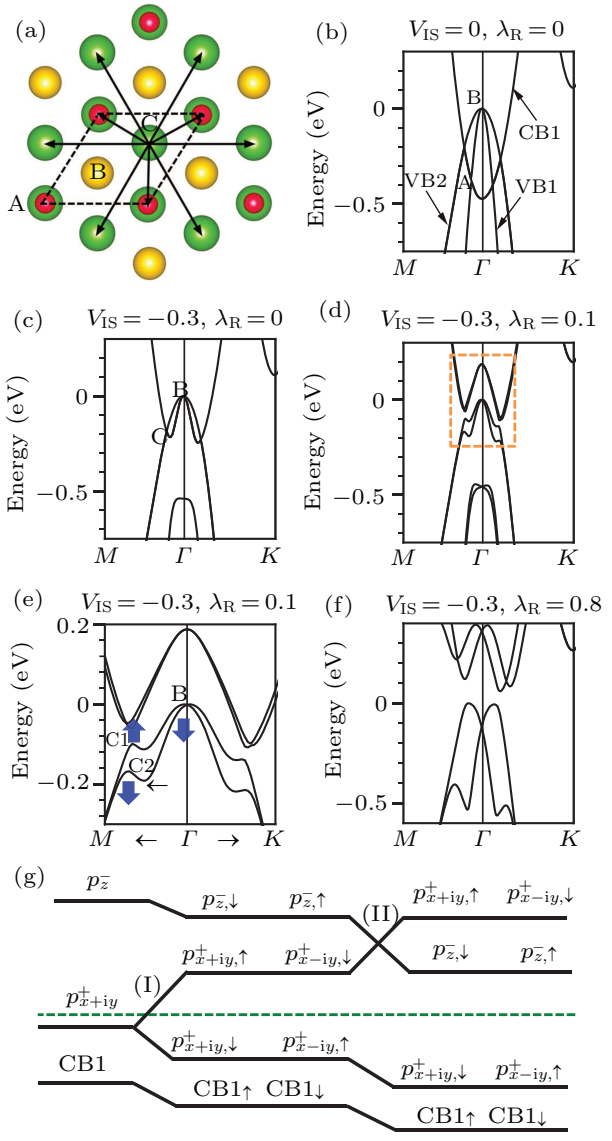


Fig. 2. (a) Top view of the Bi-bilayer/α-In_2Se_3-upward. Green, red, and yellow circles, represent Bi, Se, and In atoms, respectively, and the arrows denote the interactions considered in the tight-binding model. Dotted lines indicate the cell and A, B, C denote the high-symmetry sites of the cell. (b)–(f) The evolution of the band structures calculated by the tight-binding model as V_{IS} and λ_R vary. (e) Zoom-in band structure of the rectangle area highlighted by the orange rectangle in panel (d). The blue arrows show the trend of the band evolution with λ_R increasing. (g) The evolution of atomic basis at Γ point at stage I ($\lambda_R = 0.0$ to 0.1) and II ($\lambda_R = 0.1$ to 0.8). The superscript, $\pm$, denote the even and odd parities, respectively. The green dashed line represents the Fermi energy. Note that p_z^+ orbitals also slightly hybridize with $p^+_{x\pm\mathrm{i}y}$ due to SOC, which are not shown in the figure.

3.3. Spin–orbital-texture analysis

So far, we have clarified how the new gap is opened under the influence of the interlayer interaction and the intrinsic atomic SOC, we next analyse how this novel spin splitting forms. The eigenfunctions of the effective Rashba Hamiltonian in the basis of $|\psi_{J_z=\pm1/2}\rangle$ are expressed as $|\Phi_\pm\rangle = (1/\sqrt{2})[\pm\mathrm{i}\,\mathrm{e}^{-\mathrm{i}\theta_k}|\psi_{J_z=1/2}\rangle + |\psi_{J_z=-1/2}\rangle$, representing the upper and lower spin-split branches. According to the theory of spin–orbital texture,[16] $|\Phi_\pm\rangle$ can be rewritten in the basis of real spin $|\uparrow,\downarrow\rangle$ as

$$\begin{aligned}|\Phi_+\rangle &= \alpha_{z,k}|p_z\rangle\otimes|\mathrm{LHS}\rangle + \alpha_{r,k}|p_r\rangle\otimes|\mathrm{LHS}\rangle \\ &\quad + \alpha_{t,k}|p_t\rangle\otimes|\mathrm{RHS}\rangle, \qquad (4)\\ |\Phi_-\rangle &= \beta_{z,k}|p_z\rangle\otimes|\mathrm{RHS}\rangle + \beta_{r,k}|p_r\rangle\otimes|\mathrm{RHS}\rangle \\ &\quad + \beta_{t,k}|p_t\rangle\otimes|\mathrm{LHS}\rangle, \qquad (5)\end{aligned}$$

where $|p_r\rangle = \cos\theta_k|p_x\rangle + \sin\theta_k|p_y\rangle$, $|p_t\rangle = \cos\theta_k|p_y\rangle - \sin\theta_k|p_x\rangle$ are the radial and tangential orbital texture as shown in Figs. 3(a) and 3(b), $|\mathrm{LHS}\rangle = (1/\sqrt{2})[\mathrm{i}\,\mathrm{e}^{-\mathrm{i}\theta_k}|\uparrow\rangle + |\downarrow\rangle]$, $|\mathrm{RHS}\rangle = (1/\sqrt{2})[-\mathrm{i}\,\mathrm{e}^{-\mathrm{i}\theta_k}|\uparrow\rangle + |\downarrow\rangle]$ stand for left-handed and right-handed chiral spin textures, respectively. Equation (4) clearly demonstrates that in the upper spin–split branch, p_t orbital is coupled to the right-handed spin texture while p_r and p_z orbitals are both coupled to the left-handed spin texture, as shown in Figs. 3(a)–3(c). When considering the lower spin-split branch, the situation exactly reverses. The superposition of these opposite chirality in one band can create unique spin texture that possessing chirality reversal when the orbital character of this band change dramatically. The spin–orbital-texture analysis of the valence band for the two spin-split branch are separately displayed in Figs. 3(e)–3(h). Since p_r and p_z orbitals couple with the spin texture of same chirality, their contribution should be weighed together, noted as $p_z + p_r$. For the lower spin-split branch, the contribution of $p_z + p_r$ is larger than that of p_t in orbital texture (Fig. 3(e)) as well as spin texture (Fig. 3(f)), and thus the total spin texture possess a right-handed chirality. For the rest upper spin-split branch, $p_z + p_r$ provides larger contribution in the region near the Γ point. As the momentum moving away from the Γ point, the p_t component quickly increases and the p_z component quickly decreases (Fig. 3(g)). Therefore, as shown in Fig. 3(h), the switch of the orbital texture of the upper spin-split branch leads to the reversal of the chirality of its total spin textures. In addition, from the band evolution, it can be seen that at the valence band around the maximum, the right and left part are derived from VB1 and VB2 band, respectively, leading to the switch of their orbital texture. As the electric polarization of the ferroelectric substrate pointing downward, both the CB1 band and the conduction bands shift downward

and overlap with VB1 and VB2, resulting in different orbital texture and giving rise to a normal Rashba spin texture.

The discovered SO splitting may have following advantages. First, one of the potentially major applications of the Rashba SO splitting is the proposed spin-field-effect transistor,[41,42] which relies on the characteristic feature of two sub-bands with opposite spin–momentum chirality; this can be readily achieved via gating in our system compared with the Rashba system, because of the reversed spin textures. Secondly, the SO splitting can be switched on/off in a non-volatile fashion by reversing the orientation of the electric polarization of the ferroelectric α-In_2Se_3 substrate with the application of an external electric field. Thirdly, our systems are good semiconductors with well-defined band gaps, and the top of the valence bands are exclusively contributed by the SO splitting bands, which make the systems clean in terms of spin transport.[43]

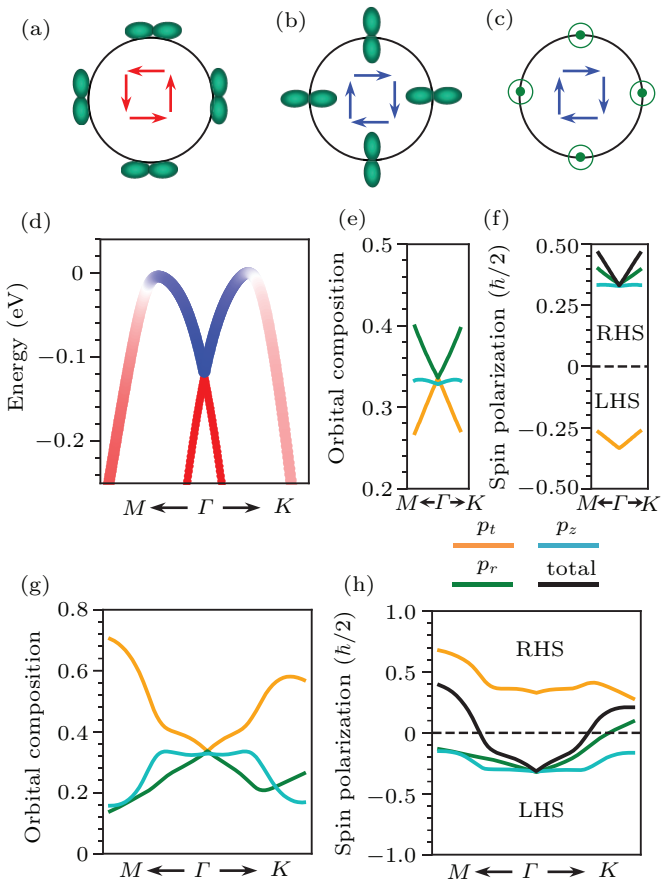


Fig. 3. (a)–(c) p_t (a), p_r (b), and p_z (c) components and their coupling with spin textures. (d) Calculated spin texture using the tight-binding model. Thick (thin) line represents upper (lower) spin-split branch. (e)–(f) Decomposed orbital composition (e) and their contribution to in-plane spin polarization (f) of the lower spin-split branch using tight-binding model. In panels (f) and (h), the sign of spin polarizaion is used to represents its chirality. (g)–(h) Similar analysis for the upper spin-split branch.

4. Conclusion

In summary, we have discovered a novel form of SO splitting in two 2D heterostructures, Bi-bilayer/In_2Se_2 and Bi-bilayer/α-In_2Se_3. Such SO splitting exhibits a Rashba-like but distinct spin textures around the valence band maximum, characterized by a reversal of spin-texture chirality in its upper spin-split branch, in contrast to the conventional Rashba systems where such reversal solely occurs from the upper to the lower spin-split branch. The ferroelectric nature of α-In_2Se_3 further enables the non-volatile control of the spin textures. Detailed analysis based on a tight-binding model reveals that such spin texture results from a synergistic effect of the interlayer interaction and the strong atomic SOC of Bi. This finding enriches the diversity of SO splitting systems and may provide new opportunity in spintronic applications.

Acknowledgment

Computational support was provided by National Supercomputing Center in Tianjin.

References

[1] Wolf S A, Awschalom D D, Buhrman R A, Daughton J M, von Molnaár S, Roukes M L, Chtchelkanova A Y and Treger D M 2001 *Science* **294** 1488
[2] Zutić I, Fabian J and Das Sarma S 2004 *Rev. Mod. Phys.* **76** 323
[3] Dresselhaus G 1955 *Phys. Rev.* **100** 580
[4] Bychkov Y A and Rashba E I 1984 *JEPT Lett.* **39** 78
[5] Hu L, Huang H, Wang Z, Jiang W, Ni X, Zhou Y, Zielasek V, Lagally M G, Huang B and Liu F 2018 *Phys. Rev. Lett.* **121** 066401
[6] Li X, Zhang S, Huang H, Hu L, Liu F and Wang Q 2019 *Nano Lett.* **19** 6005
[7] Liu K, Luo W, Ji J, Barone P, Picozzi S and Xiang H 2019 *Nat. Commun.* **10** 5144
[8] Martínez P, Högl I, González-Ruano C, Cascales J P, Tiusan C, Lu Y, Hehn M, Matos-Abiague A, Fabian J, Žutić I and Aliev F G 2020 *Phys. Rev. Appl.* **13** 014030
[9] Manchon A, Koo H C, Nitta J, Frolov S M and Duine R A 2015 *Nat. Mater.* **14** 871
[10] Nitta J, Akazaki T, Takayanagi H and Enoki T 1997 *Phys. Rev. Lett.* **78** 1335
[11] Koroteev Y M, Bihlmayer G, Gayone J E, Chulkov E V, Blügel S, Echenique P M and Hofmann P *Phys. Rev. Lett.* **93** 046403
[12] Ast C R, Henk J, Ernst A, Moreschini L, Falub M C, Pacilé D, Bruno P, Kern K and Grioni M 2007 *Phys. Rev. Lett.* **98** 186807
[13] Ishizaka K, Bahramy M S, Murakawa H, *et al.* 2007 *Nat. Mater.* **98** 186807
[14] Di Sante D, Barone P, Bertacco R and Picozzi S 2013 *Adv. Mater.* **25** 509
[15] Liebmann M, Rinaldi C, Di Sante D, *et al.* 2016 *Adv. Mater.* **28** 560
[16] Zhang H, Liu C X and Zhang S C 2013 *Phys. Rev. Lett.* **111** 066801
[17] Cao Y, Waugh J A, Zhang X W, *et al.* 2013 *Nat. Phys.* **9** 499
[18] Bawden L, Riley J M, Kim C H, *et al.* 2015 *Sci. Adv.* **1** e1500495
[19] Waugh J A, Nummy T, Parham S, Liu Q, Zhang X, Zunger A and Dessau D S 2016 *npj Quant. Mater.* **1** 16025
[20] Kresse G and Furthmüller J 1996 *Phys. Rev. B* **54** 11169
[21] Blöchl P E 1994 *Phys. Rev. B* **50** 17953
[22] Kresse G and Joubert D 1999 *Phys. Rev. B* **59** 1758
[23] Perdew J P, Burke K and Ernzerhof M 1996 *Phys. Rev. Lett.* **77** 3865
[24] Grimme S, Antony J, Ehrlich S and Krieg H 2010 *J. Chem. Phys.* **132** 154104
[25] Krukau A V, Vydrov O A, Izmaylov A F and Scuseria G E 2006 *J. Chem. Phys.* **125** 224106
[26] Methfessel M and Paxton A T 1989 *Phys. Rev. B* **40** 3616
[27] Hirahara T, Bihlmayer G, Sakamoto Y, Yamada M, Miyazaki H, Kimura S I, Blügel S and Hasegawa S 2011 *Phys. Rev. Lett.* **107** 166801
[28] Yang F, Miao L, Wang Z F, *et al.* 2012 *Phys. Rev. Lett.* **109** 016801

[29] Miao L, Wang Z F, Ming W M, *et al*. 2013 *Proc. Natl. Acad. Sci. USA* **110** 2758

[30] Kim S H, Jin K H, Park J, Kim J S, Jhi S H, Kim T H and Yeom H W 2014 *Phys. Rev. B* **89** 155436

[31] Su S H, Chuang P Y, Chen S W, *et al*. 2017 *Chem. Mater.* **29** 8992

[32] Bandurin D A, Tyurnina A V, Yu G L, *et al*. 2017 *Nat. Nanotechnol.* **12** 223

[33] Ding W J, Zhu J B, Wang Z, Gao Y, Xiao D, Gu Y, Zhang Z Z and Zhu W G 2017 *Nat. Commun.* **8** 14956

[34] Zhou Y, Wu D, Zhu Y, Cho Y, He Q, Yang X, Herrera K, Chu Z, Han Y, Downer M C, Peng H and Lai K 2017 *Nano Lett.* **17** 5508

[35] Cui C, Hu W J, Yan X X, *et al*. 2018 *Nano Lett.* **18** 1253

[36] Xiao J, Zhu H, Wang Y, Feng W, Hu Y, Dasgupta A, Han Y, Wang Y, Muller D A, Martin L W, Hu P and Zhang X 2018 *Phys. Rev. Lett.* **120** 227601

[37] Wan S, Li Y, Li W, Mao X, Zhu W and Zeng H 2018 *Nanoscale* **10** 14885

[38] Wan S, Li Y, Li W, Mao X, Wang C, Chen C, Dong J, Nie A, Xiang J, Liu Z, Zhu W and Zeng H 2018 *Adv. Funct. Mater.* **29** 1808606

[39] Koma A 1992 *Thin Solid Films* **216** 72

[40] Geim A K and Grigorieva I V 2013 *Nature* **499** 419

[41] Datta S and Das B 1990 *Appl. Phys. Lett.* **56** 665

[42] Koo H C, Kwon J H, Eom J, Chang J, Han S H and Johnson M 2009 *Science* **325** 1515

[43] Ming W, Wang Z F, Zhou M, Yoon M and Liu F 2016 *Nano Lett.* **16** 404